Water Research X 20 (2023) 100193

Contents lists available at ScienceDirect

Water Research X

journal homepage: www.sciencedirect.com/journal/water-research-x

Modulation of ultrathin nanosheet structure and nitrogen defects in graphitic carbon nitride for efficient photocatalytic bacterial inactivation

Keng-Qiang Zhong, Dong-Hua Xie [1,*], Yan-Jun Liu, Pu-Can Guo, Guo-Ping Sheng [1,*]

CAS Key Laboratory of Urban Pollutant Conversion, Department of Environmental Science and Engineering, University of Science & Technology of China, Hefei 230026, China

ARTICLE INFO

Keywords:
Photocatalytic bacterial inactivation
g-C_3N_4
Ultrathin nanosheet
Nitrogen vacancy
Bacterial capture

ABSTRACT

The efficient generation and utilization of ROSs is a key step in determining the achievement of safe drinking water by photocatalytic bacterial inactivation technology. Although graphitic carbon nitride (g-C_3N_4) serves as a green and promising photocatalyst for water disinfection, insufficient bacterial capturing capacity and serious charge recombination of pristine g-C_3N_4 extremely restrict its bactericidal activity. Herein, we develop a facile thermal exfoliation and thermal polymerization method to prepare the nitrogen-defective ultrathin g-C_3N_4 nanosheets (DUCN-500). Our results showed that ultrathin nanosheet structure greatly enhanced bacterial capturing capacity of g-C_3N_4 to increase the utilization efficiency of ROS, which contributed to the performance of DUCN-500 greatly outperforming bulk g-C_3N_4. The nitrogen defects increased ROS generation ($\cdot O_2^-$ and H_2O_2) by approximately 4.6 times, which was attributed to negative shift of the conduction band potential and rapid separation of charge carriers. The DUCN-500 could rapidly and completely inactivate *Escherichia coli* and *Bacillus subtilis* in real sewage under simulated solar irradiation, accompanied by good anti-interference capability and stability. Additionally, bacterial morphology destruction, the loss of antioxidant enzyme activity and the leakage of protein were proven to be the main mechanisms of photocatalytic sterilization. This study offers new insight into the rational design of efficient g-C_3N_4-based photocatalysts for water disinfection.

Introduction

Infectious epidemics from waterborne pathogens have caused severe threats to the health of humans worldwide (Kadoya et al., 2021; Ziemba et al., 2019). Thus, cost-effective and efficient water disinfection technologies are urgently needed to satisfy the requirements for safe drinking water. Photocatalytic bacterial inactivation as a sterilization strategy has drawn extensive attention because of its low cost, non-toxicity and outstanding sterilization effect (Zhu et al., 2022). Though photocatalysts can generate reactive oxygen species (ROSs) to attack the bacteria membrane under light irradiation (Li et al., 2012), large amount of ROSs and long residence time are required to achieve efficient inactivation efficiency (Yang et al., 2022). Furthermore, ROSs are easily scavenged by the matrix components of practical water (Li et al., 2020), thereby weakening their bactericidal activity. Therefore, the efficient generation and utilization of ROSs is a key step in determining the achievement of safe drinking water by photocatalytic bacterial inactivation technology.

The poor bacterial inactivation by photocatalysts can be ascribed to the electrostatic repulsion between negatively charged bacteria and photocatalysts, which reduces the lethality of the generated ROSs (Liu et al., 2022). Therefore, the bacterial capturing capacity of photocatalysts is crucial for bacterial inactivation. Interestingly, the strong affinity between the photocatalyst and functional groups on the bacterial cell membranes can strengthen bacterial inactivation by facilitating charge transfer of the photocatalyst-bacteria (Liang et al., 2017). Moreover, photocatalysts can tightly wrap bacteria to weaken the mobility of bacteria, thereby enhancing the inactivation effect of ROS on bacteria (Sun et al., 2019). Therefore, enhancing the bacterial capturing capacity of photocatalysts can increase the bactericidal activity.

Hydrogen peroxide (H_2O_2) has been considered an efficient and green ROS for water disinfection owing to its relatively long lifetime and safe byproducts (Sun et al., 2014). Notably, H_2O_2 can enhance bactericidal efficiency by quickly penetrating the cell membrane of bacteria (Fan et al., 2021). Moreover, H_2O_2 is difficult to react with the matrix components, thereby exhibiting excellent bactericidal activity and

* Corresponding authors.
E-mail addresses: xiedh@ustc.edu.cn (D.-H. Xie), gpsheng@ustc.edu.cn (G.-P. Sheng).
[1] Guo-Ping Sheng and Dong-Hua Xie both contributed equally.

https://doi.org/10.1016/j.wroa.2023.100193
Received 7 June 2023; Received in revised form 1 August 2023; Accepted 3 August 2023
Available online 4 August 2023

anti-interference ability in practical wastewater. Photocatalytic reduction of oxygen provides an environmentally friendly and low-energy pathway for *in situ* production of H_2O_2, which can reduce the risk and costs of the production of H_2O_2 (Li et al., 2023). As a metal-free photocatalyst, graphitic carbon nitride (g-C_3N_4) stands out with intensive attention among various candidates owing to its unique characteristics, including regulatable optical and electronic features and nontoxicity (Majdoub et al., 2020). However, insufficient bacterial capturing capacity and serious charge recombination of bulk g-C_3N_4 extremely restrict its bactericidal activity. Building a porous ultrathin structure has been considered a feasible strategy to enhance the bacterial capturing capacity of photocatalysts, which provides large specific surface area and sufficient active sites for bacterial adsorption (Ong et al., 2016; Xu et al., 2017). In addition, the intrinsic defect regulation engineering of g-C_3N_4 has been proven to be a superior strategy to suppress the recombination of charge carriers, which can not only promote charge separation, but also adjust its electronic band structure, thus enhancing the photocatalytic production of H_2O_2 (Huang et al., 2019). Elucidating the relation between defective structure and bactericidal activity is important for the rational design of efficient g-C_3N_4-based photocatalysts and further developing defect regulation strategy in g-C_3N_4 with an ultrathin structure for efficient photocatalytic bacteria inactivation is highly feasible.

Herein, we fabricated nitrogen-defective porous ultrathin g-C_3N_4 nanosheets (DUCNs) by facile thermal polymerization procedure. Without the aid of any external chemical additives (*e.g.*, templates and noxious solvents) controlling the thermal exfoliation and polymerization procedure of g-C_3N_4 can effectively adjust the ultrathin nanosheet structures and nitrogen vacancies, thereby significantly reducing the risk and costs of the DUCNs preparation. The morphological, optical and physicochemical properties of photocatalysts were characterized *via* multiple methods. The bactericidal performances of photocatalysts against two model bacteria strains, the gram-negative strain *Escherichia coli* (*E. coli*) and the gram-positive strain *Bacillus subtilis* (*B. subtilis*), were investigated. In addition, the effects of water matrix components and real water sources on the bactericidal activity and reusability of DUCN were studied. The bacterial capturing capacity and sterilization mechanisms of DUCN were also systematically studied. This work offers a facile method to prepare ultrathin g-C_3N_4 nanosheet with nitrogen defects for efficient pathogen inactivation.

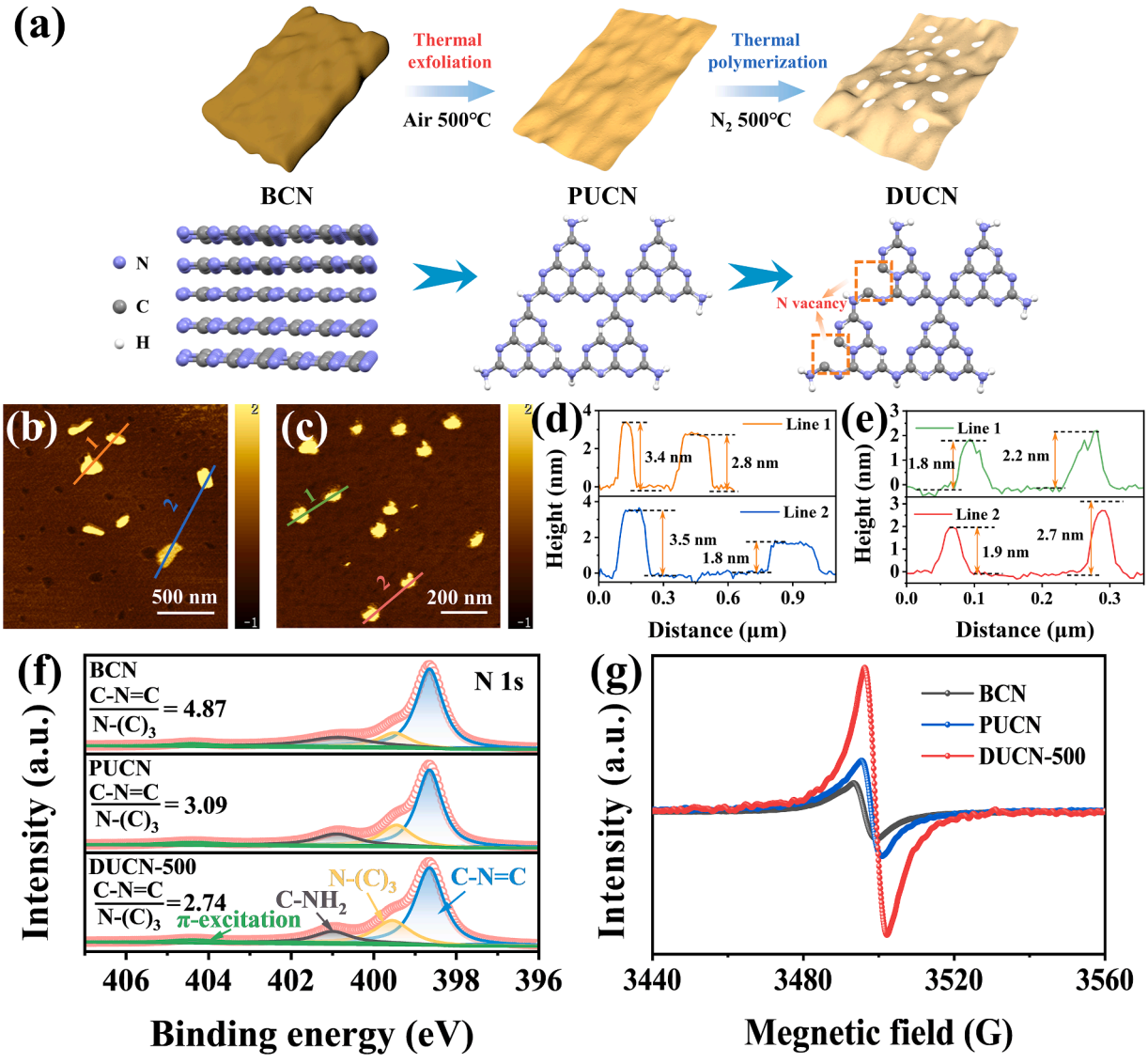

Fig. 1. (a) The preparation strategy for nitrogen-defective ultrathin DUCN nanosheets; AFM images of PUCN (b) and DUCN-500 (c); and the corresponding height profiles of PUCN (d) and DUCN-500 (e). High-resolution XPS spectra of N 1s (f) and EPR spectra(g) of various catalysts.

Results and discussion

Morphology and structure characterization

Nitrogen-defective ultrathin DUCN nanosheets were synthesized *via* the proposed thermal polymerization procedure (Fig. 1a). BCN exhibited an irregular bulk morphology with coarse surfaces (Fig. S1). For PUCN and DUCN-500, an ultrathin sheet-like morphology was observed, indicating that the thermal exfoliation validly constructed an ultrathin structure. The thickness of the samples was detected by atomic force microscopy (AFM). It can be clearly seen that PUCN and DUCN-500 possessed ultrathin nanosheet structures with thicknesses of approximately 2∼3 nm (Fig. 1b-e). Furthermore, the N_2 adsorption/desorption isotherms and pore size distribution curves (Fig. S2a-b) confirmed the coexistence of microporous and mesoporous structures in DUCN-500. The pore structural parameters and surface areas of photocatalysts are listed in Table S1. Remarkably, the surface area of DUCN-500 (213.71 $m^2\ g^{-1}$) was significantly increased compared with that of BCN (Fig. S2c), implying that the thermal polymerization could dramatically increase the specific surface area of g-C_3N_4.

As shown in Fig. S2d, all samples consisted of C, N and O elements. Moreover, Fig. 1f shows the high-resolution N 1s spectra for all photocatalysts, with four main peaks located at 398.6, 399.6, 401.0 and 404.4 eV, which were assigned to N-C=C, N-$(C)_3$, CNH_2 and π-excitation, respectively. In particular, the peak area ratio of N-C=C/N-$(C)_3$ for DUCN-500 (2.74) was dramatically reduced compared with those of BCN and PUCN, further proving the formation of V_N at the N-C=C sites during N_2 thermal polymerization (Liu et al., 2018). V_N, as the electron-enriched center, can not only facilitate electron transfer between the in-plane and interlayer of the photocatalyst, but also adjust the redox capability of the catalyst, thereby reducing the reaction activation energy barrier. Furthermore, electron paramagnetic resonance (EPR) intensity of the photocatalysts followed the order of DUCN-600 > DUCN-500 > DUCN-400 >PUCN > BCN, suggesting that the intrinsic defect degree of g-C_3N_4 could be effectively adjusted by thermal polymerization in N_2 (Figs. 1g and S2e). Fourier transform infrared (FTIR) spectra (Fig. S2f) of all photocatalysts exhibited similar adsorption peaks at 805, 1100–1700 and 3000–3400 cm^{-1} were corresponding to the s-triazine unit, C—N heterocycles and N—H groups, respectively. The FTIR results suggested that the modified samples maintained the basic triazine structure of g-C_3N_4.

Optical properties and electronic structures

The ultraviolet−visible absorption spectra and the relevant bandgaps of photocatalysts are depicted in Fig. S3a-b. Furthermore, the corresponding valence band potentials of BCN, PUCN and DUCN-500 were calculated to be 1.47, 1.44 and 1.29 V (*vs*. NHE, pH=7), respectively (Fig. S3c) (Yu et al., 2017). Moreover, the detailed band structures of samples are illustrated in Fig. S3d, confirming that the photocatalysts could meet the thermodynamic demands for the production of $\cdot O_2^-$ and H_2O_2 by photocatalytic oxygen reduction reaction (Liu et al., 2021). Notably, the conduction band (CB) potential of DUCN-500 was negatively shifted by 0.25 V compared to that of BCN, which was attributed to the introduction of nitrogen defect. In Fig. S4a, the photoluminescence (PL) intensities of these catalysts were in the order of DUCN-500 < PUCN < BCN, suggesting that nitrogen defects effectively promoted the separation of photogenerated charge carriers in g-C_3N_4. Compared with BCN and PUCN, DUCN-500 displayed slower PL decay kinetics and the longest average lifetime of 3.55 ns, outperforming PUCN and BCN (Fig. S4b and Table S2), confirming that the introduction of N defects could effectively suppress the rapid recombination of photoexcited electron holes. Furthermore, DUCN-500 photoelectrode demonstrated a higher photocurrent density than BCN and PUCN (Fig. S4c), confirming that N defects could accelerate the transfer of charge carriers. Overall, N defects not only improve the reductive capability of CB, but also promote the separation of photogenerated charge carriers, showing great potential for photocatalytic sterilization.

Photocatalytic bactericidal performance

For the photocatalytic inactivation of *E. coli*, the BCN and PUCN displayed poor inactivation efficiency with 2.4 and 3.5 $\log_{10}$ CFU/mL for *E. coli* within 90 min, respectively (Fig. 2a). Compared with the DUCN-400 and DUCN-600, DUCN-500 demonstrated the highest sterilization performance with complete inactivation of 7.0 $\log_{10}$ CFU/mL for *E. coli* within 60 min (Fig. S5a). For the photocatalytic inactivation of *B. subtilis*, the complete inactivation of 7.1 $\log_{10}$ CFU/mL for *B. subtilis* was achieved by DUCN-500 within 75 min (Figs. 2b and S5b), outpacing the DUCN-400 and DUCN-600 photocatalysts. The above results confirmed that DUCN-500 with the ultrathin nanostructure and N defects could obviously strengthen the bactericidal activity. Notably, DUCN-500 photocatalytic sterilization fully restrained the reactivation of *E. coli* and *B. subtilis* within 7 days (Fig. S6a-b), suggesting that DUCN-500 could rapidly and completely inactivate bacteria. Furthermore, the photocatalytic sterilization activity of DUCN-500 could be comparable with those of recently reported g-C_3N_4-based photocatalysts (Table S3), implying its superior bactericidal efficiency. Compared with other existing and emerging AOP-based disinfection systems, the inactivation efficiency and cost of the DUCN-500 sterilization system were competitive (Table S4), which can be a potential and low-cost technology for bacterial inactivation.

The influences of HA and inorganic anions were investigated to evaluate the sterilization efficiency of DUCN-500 in complicated water matrices. As the dosage of HA increased from 0.5 to 10 mg/L, the inactivation of *E. coli* was slightly inhibited (Fig. S6c), which could be attributed to the consumption of ROS by high concentration of HA. Moreover, the bactericidal efficiency for *E. coli* was slightly restrained in the presence of CH_3COO^-, SO_4^{2-}, NO_3^- and Cl^- (Fig. S6d). Moreover, the photocatalytic sterilization performance and structural stability of DUCN-500 displayed no distinct decline and difference after 5 cycles (Figs. S6e and S7), revealing its good reusability and stability. Moreover, photocatalytic bacterial inactivation by the DUCN-500 was also examined in actual water systems, containing ground water (GW), river water (RW) and secondary effluent (SE). The water quality parameters of real sewage are summarized in Table S5. As displayed in Fig. 2c, 7.0 $\log_{10}$ CFU/mL of *E. coli* could be inactivated within 60 and 75 min by DUCN-500 in the GW, RW and SE, respectively. In addition, 7.0 $\log_{10}$ CFU/mL of *B. subtilis* cells could be inactivated within 75 min by DUCN-500 in GW and RW, respectively, while complete inactivation of 7.1 $\log_{10}$ CFU/mL for *B. subtilis* was achieved by DUCN-500 within 90 min in SE (Fig. 2d). The slightly decreased bactericidal ability might be caused by matrix components of practical water. In summary, DUCN-500 showed great prospects for photocatalytic bacterial inactivation in practical water treatment.

Working reactive species

The quenching experiments are conducted to evaluate the contribution of specific ROSs in photocatalytic sterilization by DUCN-500. Specifically, ammonium oxalate, Cr (VI), isopropanol, L-histidine, 4-hydroxy-TEMPO (TEMPOL) and catalase (CAT) were used as the scavengers for h^+, e^-, ·OH, $^1O_2$, $\cdot O_2^-$ and H_2O_2, respectively. The dosages of these scavengers used in this study had no influence on bacterial growth (Fig. S8a). As displayed in Fig. 3a, little inhibition of sterilization performance with the addition of isopropanol and L-histidine, respectively, demonstrating that ·OH and $^1O_2$ was not directly involved in sterilization. Furthermore, with the addition of ammonium oxalate, the bactericidal efficiencies decreased slightly, revealing that h^+ played a moderate role in sterilization. More strikingly, the addition of Cr (VI), TEMPOL and CAT obviously reduced the bactericidal efficiencies, revealing the important role of e^-, $\cdot O_2^-$ and H_2O_2 in photocatalytic

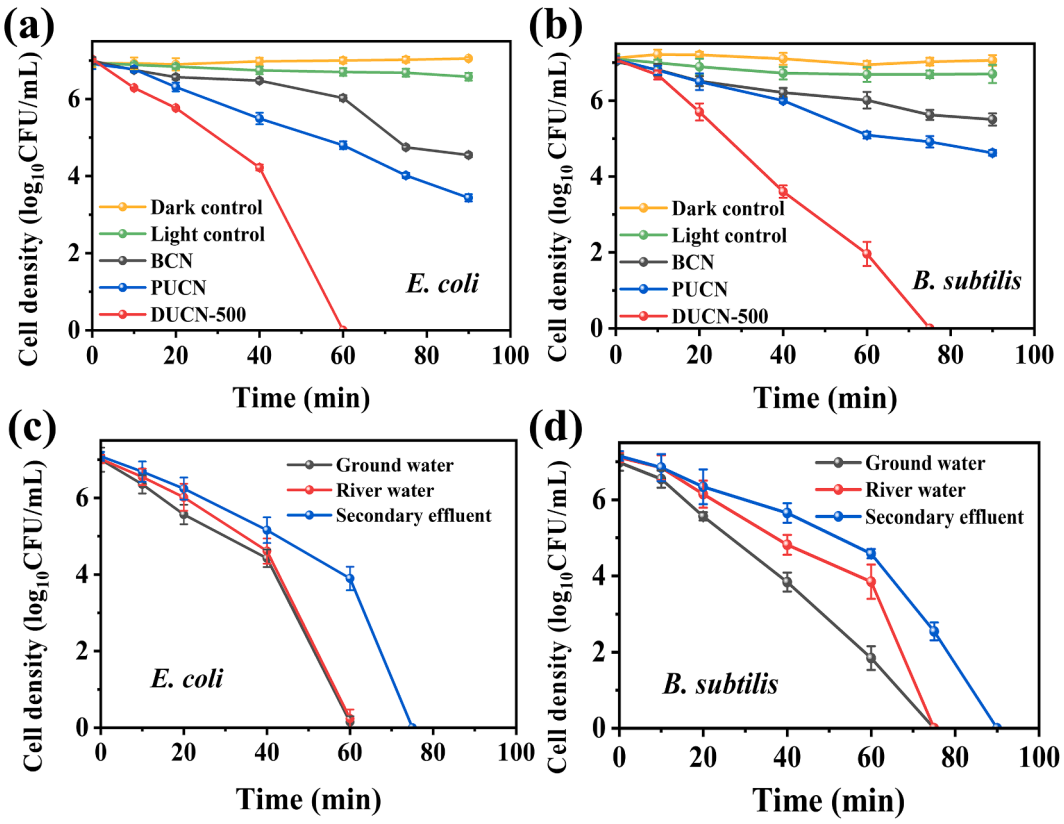

Fig. 2. Photocatalytic inactivation efficiencies toward (a) *E. coli* and (b) *B. subtilis* using as-synthesized photocatalysts; Photocatalytic inactivation of (c) *E. coli* and (d) *B. subtilis* by DUCN-500 in authentic water matrices.

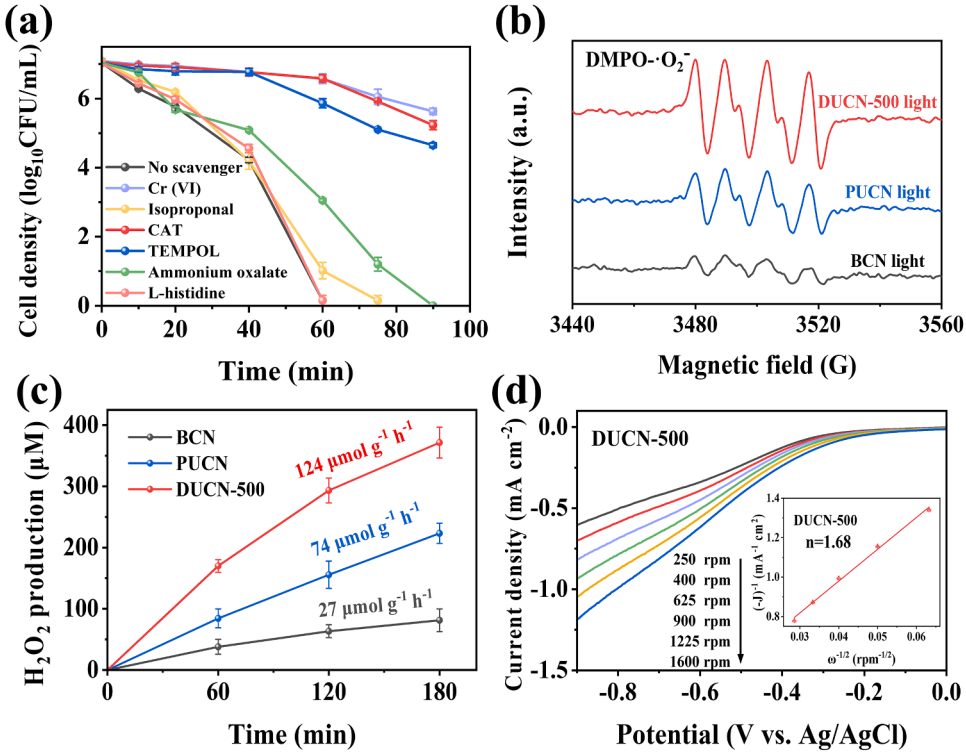

Fig. 3. (a) Photocatalytic bactericidal efficiencies of *E. coli* by DUCN-500 with different scavengers. (0.5 mM ammonium oxalate, 0.1 mM Cr (VI), 0.5 mM isopropanol, 0.5 mM L-histidine, 2 mM TEMPOL, 100 U/mL CAT). (b) EPR spectra of DMPO-·O_2^- for BCN, PUCN and DUCN-500 suspensions under light irradiation; (c) H_2O_2 concentrations photogenerated by BCN, PUCN and DUCN-500; (d) LSV curves of DUCN-500 measured on RDE at various rotating speeds, inset: the corresponding *K-L* plots.

sterilization. These results demonstrated that the contribution of reactive species for bacterial inactivation followed the order of $H_2O_2 > h^+ > {}^1O_2$, with H_2O_2 played the major role in bacterial inactivation (Fig. S8b). Moreover, the photocatalytic bactericidal efficiency was almost completely restrained under Ar (Fig. S8c), indicating that O_2 was the precursor of $\cdot O_2^-$ and H_2O_2 in the photocatalytic process. The above

results assumed that the efficient bactericidal activity of DUCN-500 was mainly due to the generation of H_2O_2, and $\bullet O_2^-$ was a critical intermediate in the formation of H_2O_2, as described in Eqs. (1)–(3):

$$O_2 + e^- \rightarrow \cdot O_2^- \quad (1)$$

$$\cdot O_2^- + e^- + 2H^+ \rightarrow H_2O_2 \quad (2)$$

$$O_2 + 2e^- + 2H^+ \rightarrow H_2O_2 \quad (3)$$

As depicted in Fig. S9a-b, no DMPO-·OH and TEMP-$^1O_2$ signals for DUCN-500 were obtained under dark conditions and light irradiation. Notably, DUCN-500 exhibited the strongest signal intensity of DMPO-$\cdot O_2^-$ and the highest concentration of $\cdot O_2^-$ compared with BCN and PUCN (Figs. 3b and S9c). Furthermore, DUCN-500 showed the highest H_2O_2 generation rate of 124 μmol g^{-1} h^{-1} (Fig. 3c), which was approximately 4.6 and 1.7 times higher than those of BCN and PUCN, respectively. Fig. 3d shows the linear sweep voltammetry curves of DUCN-500, and the electron transfer number of DUCN-500 was calculated to be 1.68 (inset of Fig. 3d), indicating that both indirect e^- and direct $2e^-$ transfer pathways existed in oxygen reduction under the photocatalysis of DUCN-500. Overall, the N defects can effectively separate charge carriers and adjust the reductive capability of CB to promote more generation of H_2O_2, thereby greatly enhancing the photocatalytic bactericidal activity for DUCN-500.

Bacteria-photocatalyst contact

As shown in Fig. 4a, few bacteria adhered to the surface of BCN, while most *E. coli* were captured by PUCN and DUCN-500 and tightly adhered to their surface (Fig. 4b-c), which was mainly contributed by the ultrathin nanostructure. Furthermore, the mechanism of interaction between photocatalysts and bacteria was investigated by extended Derjaguin-Landau-Verwey-Overbeek (XDLVO) theory. The hydrodynamic diameter, zeta potential, contact angle and Hamaker constant of the photocatalysts were listed in Table S6. The positive or negative interaction energy indicated a repulsive or attractive force between *E. coli* and the catalyst, respectively. Because the Lewis acid-base interaction energy (V_{AB}) was significantly lower than the van der Waals attraction (V_A) and the electrical double layer electrostatic interaction energy (V_R), the total interaction energy (V_T) was dominated by V_A and V_R. Fig. 4d illustrates that the V_T of BCN-*E. coli* system was strongly affected by the electrostatic repulsive force, and the maximum energy barrier was 21.6 K_BT ($h = 0.5$ nm). Due to the high energy barrier of BCN-*E. coli* system, the bacteria were difficult to adhere to the surfaces of pristine bulk g-C_3N_4. In contrast, the energy barrier was completely screened by weakened electrical double layer compression for both PUCN-*E. coli* and DUCN-500-*E. coli* system, and the corresponding energy barriers were −50.2 and −54.6 K_BT (Fig. 4e and f), respectively. Such trends indicated that the bacterial cells might readily adhere to the surface of g-C_3N_4 nanosheets, which was consistent with the scanning electron microscopy (SEM) images. The XDLVO results further proved that the construction of the ultrathin nanosheet structure greatly weakened the energy barrier to promote the tight contact between the bacteria and photocatalysts.

Bacterial inactivation mechanism

The *E. coli* showed a preserved and smooth cell membrane before the photocatalytic treatment (Fig. 5b). During the photocatalytic inactivation process (Fig. 5c-e), the membrane surface of *E. coli* was seriously deformed and ruptured with distinct holes, indicating that ROS could cause serious damage to the membrane. The bacterial morphology images were in good agreement with the plate photographs of *E. coli* at the different phases of the photocatalytic bactericidal process (Fig. 5a).

The intracellular relative ROS levels gradually increased with the progression of the photocatalytic inactivation process (Fig. 5f), whereas the enhancement of intracellular relative ROS levels was not observed under the dark control. The above results confirmed that ROS could continuously attack the bacteria and cause damage to the bacterial antioxidative defense system. Superoxide dismutase (SOD) and CAT can quench $\cdot O_2^-$ and H_2O_2, respectively, thus preventing the oxidative damage of cells (Xiao et al., 2020). Insignificant activities of CAT and SOD were observed under the dark control, while both CAT and SOD activities were rapidly enhanced within the first 40 min under light irradiation and then gradually reduced (Fig. 5g-h). With the accumulation of ROS, CAT and SOD were greatly consumed, and the

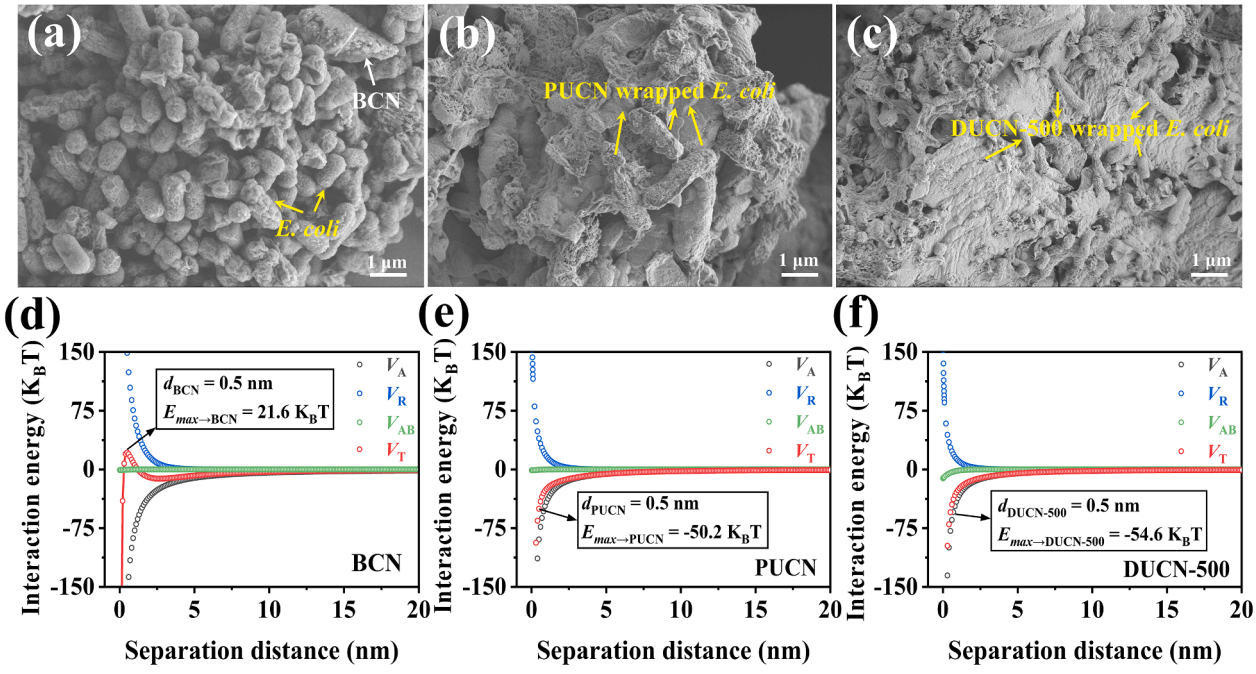

Fig. 4. SEM images of *E. coli* after mixing with (a) BCN, (b) PUCN and (c) DUCN-500; interaction energy profiles between *E. coli* and (d) BCN, (e) PUCN and (f) DUCN-500 as a function of separation distance.

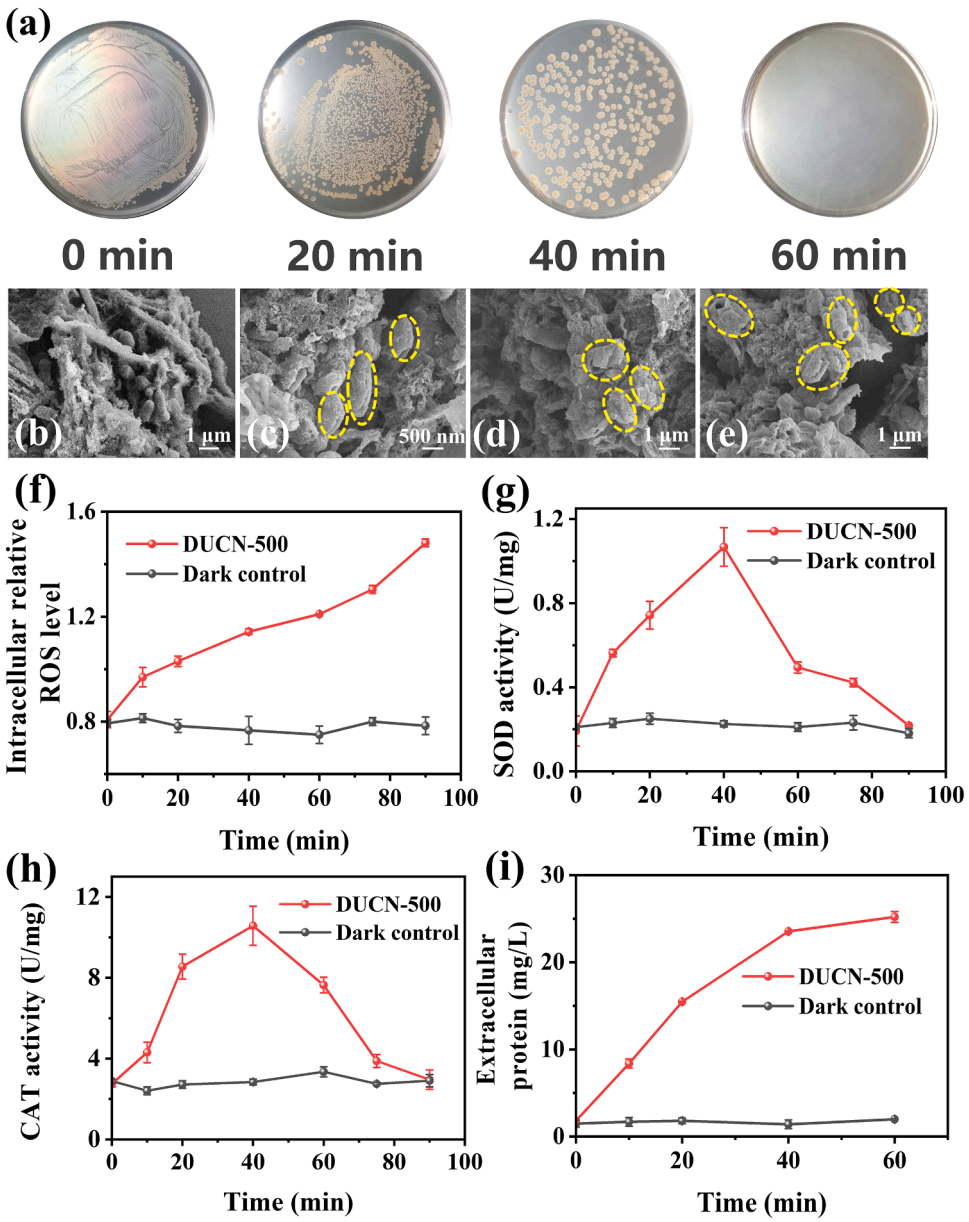

Fig. 5. (a) Photographs of *E. coli* at the different phases of photocatalytic inactivation; SEM images of *E. coli* after photocatalytic treatment with DUCN-500 for (b) 0 min, (c) 20 min, (d) 40 min, and (e) 60 min; (f) intracellular relative ROS level; (g) SOD activity; (h) CAT activity; and (i) extracellular protein during the photocatalytic inactivation process.

antioxidative defense system of bacteria was destroyed, resulting in massive inactivation of bacteria. In contrast to the dark control, the contents of extracellular protein continuously increased during photocatalytic inactivation (Fig. 5i). This phenomenon proved that ROSs effectively damaged the cell membrane and caused the leakage of intracellular substances, thereby resulting in massive inactivation of bacteria.

Conclusion

In this study, an outstanding bactericidal performance was achieved using the nitrogen-defective porous ultrathin g-C_3N_4 nanosheet. The construction of ultrathin nanosheet structures enhanced the bacterial capturing capacity of g-C_3N_4, thereby enhancing the effective usage of ROSs for photocatalytic bacterial inactivation. In addition, nitrogen defects in the catalyst not only boosted the carrier separation and accelerated the charge transportation, but also produce more $\cdot O_2^-$ and H_2O_2, hence improving the photocatalytic bactericidal performance. The tight bacteria-photocatalyst contact and enhanced production of ROS greatly strengthened the sterilization activity in actual water and anti-interference capability of g-C_3N_4. Furthermore, the membrane damage and leakage of protein were caused by the major ROS, resulting in the death of bacteria. This work provides novel ideas to prepare low-cost and efficient g-C_3N_4-based photocatalysts for bacterial inactivation.

Experimental methods

Synthesis of porous ultrathin and nitrogen-deficient g-C_3N_4

Bulk g-C_3N_4 was prepared by one-step thermal polymerization. Briefly, 10 g melamine was heated at 550 °C for 4 h with a heating rate of 5 °C min^{-1} in a muffle furnace. The prepared powders were labeled BCN.

Porous ultrathin g-C_3N_4 nanosheets were synthesized *via* a facile thermal exfoliation method. In brief, 1 g of BCN was placed in a crucible

and calcined at 500 °C for 4 h with a heating rate of 5 °C min^{-1} under air conditions. The obtained porous ultrathin g-C_3N_4 nanosheets were represented as PUCN.

The defective ultrathin g-C_3N_4 nanosheets, named DUCN, were fabricated with the following step. First, 0.5 g of the as-prepared PUCN was further calcined at various temperatures between 400 and 600 °C for 4 h under a nitrogen atmosphere with a heating rate of 5 °C min^{-1}. For simplicity, these catalysts were denoted as DUCN-T, where T indicates the carbonization temperature. The chemical details and characterization of the prepared catalysts are described in the Supporting Information.

Photocatalytic bacterial inactivation

E. coli and *B. subtilis* were used as the model bacteria of the gram-negative strain and gram-positive strain, respectively. The bacteria were incubated in 100 mL nutrient broth for 15 h at 37 °C and subsequently collected through centrifugation at 6000 rpm for 5 min. Afterwards, sterile buffer solution (8 g/L NaCl, 0.2 g/L KCl, 1.44 g/L Na_2HPO_4 and 0.24 g/L KH_2PO_4, initial pH 7.0) was used to wash the bacterial pellets twice. 50 mg photocatalyst was dispersed in 50 mL of bacterial solution (10^7 CFU/mL, initial pH of 7.0) and then stirred for 90 min at room temperature under simulated sunlight irradiation (with an Air Mass 1.5 filter, Beijing China Education Au-light Co., China) at a light intensity of 150 mW/cm^2. At various time intervals, 1 mL of the sample suspension was collected and diluted with a sterile buffer solution. Finally, 100 μL of the diluted sample suspension was spread onto nutrient agar plates and incubated at 37 °C for 24 h to count the number of viable cells. For comparison, the light control groups were treated under light irradiation only without catalysts, and the dark control groups were treated in the dark with the catalyst. All photocatalytic bactericidal experiments were carried out in triplicate. The ROS detection methods, reactivation experiments of bacteria after photocatalytic sterilization, antioxidant enzyme activities tests, extracellular protein quantification and intracellular ROS relative levels detection are provided in the Supporting Information. The interaction between g-C_3N_4 and *E. coli* was calculated by the extended XDLVO theory, which is illustrated in the Supporting Information.

Reactivation experiments

The bacterial inactivation effect of photocatalytic sterilization was assessed by the reactivation experiments using OD600 and plate culture method (Wang et al., 2021; Zhang et al., 2015). In brief, the 100 μL samples treated with photocatalytic sterilization and nutrient broth were muddle in 96-well microplates via shaking at 37 °C. The absorbance at 600 wavelength was determined on a microplate reader (Spectra Max M2e, Molecular Devices Co., USA). Besides, the 100 μL samples treated with photocatalytic sterilization were incubated into 20 mL nutrient broth for one week at 37 °C. At days 1, 3, 5 and 7, 100 μL of sample suspension was spread onto Nutrient Agar plates and incubated at 37 °C for 24 h to count viable cell. 100 μL of sterile buffer solution and 100 μL nutrient broth were used as negative controls.

Photoelectrochemical measurements

3 mg of the as-prepared composites was dispersed in a mixture containing 500 μL deionized water, 500 μL ethanol and 20 μL Nafion solution (5 wt.%) *via* ultrasonic treatment for 30 min to achieve a homogeneous catalyst suspension. Afterward, the above suspension was dropped onto the working electrode and dried to constitute a film. The photoelectrochemical tests were performed on a CHI760E electrochemical workstation (Chenhua Co., China) in a three-electrode system containing a working electrode, a platinum mesh counter electrode and an Ag/AgCl reference electrode. The working electrode was fabricated by coating photocatalysts on the F-doped SnO_2 (FTO) electrode (mass loading: 0.3 mg cm^{-2}). A Xenon lamp (300 W) was applied as the light source to irradiate the photocatalyst system. The transient photocurrent response curves were tested in oxygen-saturated 0.5 M Na_2SO_4 electrolyte. The measurement details of the H_2O_2 concentration are provided in the Supporting Information. To evaluate the oxygen reduction reaction (ORR) activity of catalysts, linear sweep voltammetry (LSV) tests were conducted on a rotating disk electrode (RDE) with a glassy carbon electrode as the working electrode. The homogeneous catalyst suspension was added dropwise onto the glassy carbon electrode (mass loading: 0.2 mg cm^{-2}). The LSV curves were collected from −0.9 to 0.2 V (*vs.* Ag/AgCl) at a scan rate of 10 mV s^{-1} with different rotation rates from 250 to 1600 rpm in 0.5 M oxygen-saturated Na_2SO_4 solution. The *n* in the ORR was achieved by Koutecky-Levich (*K-L*) equations (Zhong et al., 2020):

$$\frac{1}{J} = \frac{1}{J_k} + \frac{1}{B\omega^{0.5}} \tag{4}$$

$$B = 0.62nFAD_0^{2/3}\nu^{-1/6}C_0 \tag{5}$$

where J and J_k indicate the current density and the kinetic current density, respectively; ω represents the electrode rotation rate; F is the Faraday constant (96,485 C mol^{-1}); A is the area of the glassy carbon electrode; D_0 indicates the diffusion coefficient of O_2 (2.7×10^{-5} cm^2 s^{-1}); ν indicates the kinetic viscosity of the solution (0.01 cm^2 s^{-1}); and C_0 indicates the bulk concentration of oxygen (1.2×10^{-3} mol L^{-1}).

Data availability

Data will be made available on request.

CRediT authorship contribution statement

Keng-Qiang Zhong: Conceptualization, Methodology, Validation, Data curation, Writing – original draft. **Dong-Hua Xie:** Validation, Investigation, Formal analysis. **Yan-Jun Liu:** Investigation, Formal analysis. **Pu-Can Guo:** Validation, Investigation. **Guo-Ping Sheng:** Conceptualization, Resources, Supervision, Project administration, Funding acquisition, Writing – review & editing.

Declaration of Competing Interest

The authors declare that they have no known competing financial interests or personal relationships that could have appeared to influence the work reported in this paper.

Acknowledgments

The authors wish to thank the Anhui Province Key Research and Development Program (2023t07020017), the National Natural Science Foundation of China (51825804), the Fundamental Research Funds for the Central Universities (WK2400000001) and the CAS Key Laboratory of Urban Pollutant Conversion Joint Research Fund (KLUPC-2022-4) for the support of this study.

Supplementary materials

Supplementary material associated with this article can be found, in the online version, at doi:10.1016/j.wroa.2023.100193.

References

Fan, W., Cui, J., Li, Q., Huo, Y., Xiao, D., Yang, X., Yu, H., Wang, C., Jarvis, P., Lyu, T., Huo, M., 2021. Bactericidal efficiency and photochemical mechanisms of micro/nano bubble–enhanced visible light photocatalytic water disinfection. Water Res. 203, 117531.

Huang, Y., Li, D., Fang, Z., Chen, R., Luo, B., Shi, W., 2019. Controlling carbon self-doping site of g-C_3N_4 for highly enhanced visible-light-driven hydrogen evolution. Appl. Catal. B Environ. 254, 128–134.

Kadoya, S.S., Nishimura, O., Kato, H., Sano, D., 2021. Predictive water virology using regularized regression analyses for projecting virus inactivation efficiency in ozone disinfection. Water Res. X 11, 100093.

Li, D., Yu, P., Zhou, X., Kim, J.H., Zhang, Y., Alvarez, P.J.J., 2020. Hierarchical $Bi_2O_2CO_3$ wrapped with modified graphene oxide for adsorption-enhanced photocatalytic inactivation of antibiotic resistant bacteria and resistance genes. Water Res. 184, 116157.

Li, R., Zheng, M., Zhou, X., Zhang, D., Shi, Y., Li, C., Yang, M., 2023. Carbon vacancies in porous g-C_3N_4 nanosheets induced robust H_2O_2 production for highly efficient photocatalysis-self-Fenton system for metronidazole degradation. Chem. Eng. J. 464, 142584.

Li, Y., Zhang, W., Niu, J., Chen, Y., 2012. Mechanism of photogenerated reactive oxygen species and correlation with the antibacterial properties of engineered metal-oxide nanoparticles. ACS Nano 6 (6), 5164–5173.

Liang, J., Liu, F., Deng, J., Li, M., Tong, M., 2017. Efficient bacterial inactivation with Z-scheme AgI/Bi_2MoO_6 under visible light irradiation. Water Res. 123, 632–641.

Liu, J., Fang, W., Wei, Z., Qin, Z., Jiang, Z., Shangguan, W., 2018. Efficient photocatalytic hydrogen evolution on N-deficient g-C_3N_4 achieved by a molten salt post-treatment approach. Appl. Catal. B: Environ. 238, 465–470.

Liu, J., Zhu, Y., Chen, J., Butenko, D.S., Ren, J., Yang, X., Lu, P., Meng, P., Xu, Y., Yang, D., Zhang, S., 2021. Visible-light driven rapid bacterial inactivation on red phosphorus/titanium oxide nanofiber heterostructures. J. Hazard. Mater. 413, 125462.

Liu, Y., Dong, W., Shen, S., Meng, F., Wang, J., Yang, K., Lin, D., 2022. Enhancement of *E. coli* inactivation by photosensitized erythrosine-based solar disinfection under weakly acidic conditions. Water Res. 212, 118125.

Majdoub, M., Anfar, Z., Amedlous, A., 2020. Emerging chemical functionalization of g-C_3N_4: covalent/noncovalent modifications and applications. ACS Nano 14 (10), 12390–12469.

Ong, W.J., Tan, L.L., Ng, Y.H., Yong, S.T., Chai, S.P., 2016. Graphitic carbon nitride (g-C_3N_4)-based photocatalysts for artificial photosynthesis and environmental remediation: are we a step closer to achieving sustainability? Chem. Rev. 116 (12), 7159–7329.

Sun, H., Gao, N., Dong, K., Ren, J., Qu, X., 2014. Graphene quantum dots-band-aids used for wound disinfection. ACS Nano 8 (6), 6202–6210.

Sun, H., Wang, J., Jiang, Y., Shen, W., Jia, F., Wang, S., Liao, X., Zhang, L., 2019. Rapid aerobic inactivation and facile removal of *Escherichia coli* with amorphous zero-valent iron microspheres: indispensable roles of reactive oxygen species and Iron corrosion products. Environ. Sci. Technol. 53 (7), 3707–3717.

Wang, L., Ye, C., Guo, L., Chen, C., Kong, X., Chen, Y., Shu, L., Wang, P., Yu, X., Fang, J., 2021. Assessment of the UV/chlorine process in the disinfection of *Pseudomonas aeruginosa*: efficiency and mechanism. Environ. Sci. Technol. 55 (13), 9221–9230.

Xiao, K., Wang, T., Sun, M., Hanif, A., Gu, Q., Tian, B., Jiang, Z., Wang, B., Sun, H., Shang, J., Wong, P.K., 2020. Photocatalytic bacterial inactivation by a rape pollen-MoS_2 biohybrid catalyst: synergetic effects and inactivation mechanisms. Environ. Sci. Technol. 54 (1), 537–549.

Xu, J., Wang, Z., Zhu, Y., 2017. Enhanced visible-light-driven photocatalytic disinfection performance and organic pollutant degradation activity of porous g-C_3N_4 nanosheets. ACS Appl. Mater. Interfaces 9 (33), 27727–27735.

Yang, L., Yang, H., Yin, S., Wang, X., Xu, M., Lu, G., Liu, Z., Sun, H., 2022. Fe single-atom catalyst for efficient and rapid Fenton-like degradation of organics and disinfection against bacteria. Small 18 (9), 2104941.

Yu, H., Shi, R., Zhao, Y., Bian, T., Zhao, Y., Zhou, C., Waterhouse, G.I.N., Wu, L.Z., Tung, C.H., Zhang, T., 2017. Alkali-assisted synthesis of nitrogen deficient graphitic carbon nitride with tunable band structures for efficient visible-light-driven hydrogen evolution. Adv. Mater. 29 (16), 1605148.

Zhang, S., Ye, C., Lin, H., Lv, L., Yu, X., 2015. UV Disinfection induces a Vbnc state in *Escherichia coli* and *Pseudomonas aeruginosa*. Environ. Sci. Technol. 49 (3), 1721–1728.

Zhong, K., Wang, Y., Wu, Q., You, H., Zhang, H., Su, M., Liang, R., Zuo, J., Yang, S., Tang, J., 2020. Highly conductive skeleton graphitic-C_3N_4 assisted Fe-based metal-organic frameworks derived porous bimetallic carbon nanofiber for enhanced oxygen-reduction performance in microbial fuel cells. J. Power Sources 467, 228313.

Zhu, Z.H., Liu, Y., Song, C., Hu, Y., Feng, G., Tang, B.Z., 2022. Porphyrin-based two-dimensional layered metal–organic framework with sono-/photocatalytic activity for water decontamination. ACS Nano 16 (1), 1346–1357.

Ziemba, C., Larivé, O., Deck, S., Huisman, T., Morgenroth, E., 2019. Comparing the anti-bacterial performance of chlorination and electrolysis post-treatments in a hand washing water recycling system. Water Res. X 2, 100020.